Accurate Calculation of the Phenyl Radical's Magnetic Inequivalency, Relative Orientations of Its Spin Hamiltonian Tensors, and Its Electronic Spectrum

Saba M. Mattar*

Department of Chemistry and Centre for Laser, Atomic and Molecular Sciences, University of New Brunswick, Fredericton, New Brunswick, Canada E3B 6E2

Received: September 5, 2006; In Final Form: October 30, 2006

The phenyl radical's electronic structure, magnetic inequivalency, spin Hamiltonian tensor components, and the relative orientation of their principal axes are computed by Neese's coupled-perturbed Kohn−Sham hybrid density functional (CPKS-HDF) technique in a moderate amount of time without resorting to expensive post-Hartree−Fock techniques. The **g** tensor component values are in excellent agreement with those determined experimentally and differ by less than 370 ppm. The computed hydrogen nuclear hyperfine tensors, **A**(^{1}H), are also found to be in very good agreement with their experimental counterparts. The correlation of the radical's electronic structure with its **g** and **A** numerical values corroborates that it has a $^2A_1$ ground state. In accordance with our previous studies on the equivalency of planar radicals that possess C_{2v} symmetry, the in-plane **g** and **A**(^{1}H) principal axes should not be parallel to one another. Consequently, the spatially equivalent *ortho* ($^1H_2$, $^1H_6$) and *meta* ($^1H_3$, $^1H_5$) proton pairs should be magnetically inequivalent. This was confirmed in both the present computations and the simulation of the EPR solid-state spectrum. To the best of our knowledge, this is the first aromatic in-plane σ-type radical whose magnetic inequivalency is studied both computationally and experimentally. To properly interpret the radical's electronic excitation spectra, the spectroscopy-oriented dedicated difference configuration interaction (SORCI) procedure was employed. Aside from a slight overestimation, the method seems to be capable of reproducing the $\mathbf{C_6H_5}\bullet$ electronic vertical excitation energies in the range of 0−50 000 cm^{-1}. These vertical excitations, in conjunction with the corresponding orbit and spin orbit matrix elements, were also used to compute the **g** tensor components, employing the sum-over-states technique. Due to the limited number of computed roots and excited states, the results were marginally inferior to those obtained using the CPKS-HDF method.

I. Introduction

Aromatic organic free radicals, such as the phenyl radical ($\mathbf{C_6H_5}\bullet$) shown in Figure 1, are of vital importance in a large variety of chemical reactions. They are essential transient intermediates in the processing of organic pollutants and in the incineration of organic compounds.[1,2] In addition, they also play significant roles in oncogenesis and in tumor therapy by photoirradiation.[3]

$\mathbf{C_6H_5}\bullet$ is of additional interest because it is believed to be a precursor in the synthesis of polyaromatic hydrocarbons (PAHs). PAHs and their formation reaction mechanisms have lately been the focus of attention of chemists, spectroscopists, and astrophysicists as significant chemical compounds of interstellar space.[4] The formation of PAHs is believed to begin with ions and molecules containing two or three carbon atoms. It is suggested that the first aromatic transient intermediate formed along this reaction pathway is $\mathbf{C_6H_5}\bullet$.[5]

The phenyl radical has been studied by a variety of spectroscopic techniques to probe its rotational, vibrational, and electronic structure in the gas phase and in the solid state when isolated in rare gas matrices. In the gas phase, $\mathbf{C_6H_5}\bullet$ was generated by a direct current discharge from a mixture of argon and benzene in a pulsed supersonic molecular beam. Its microwave spectra at millimeter wavelengths displayed 14 rotational transitions between 9 and 40 GHz and over 50 transitions between 150 and 330 GHz, each split by spin doubling.[6]

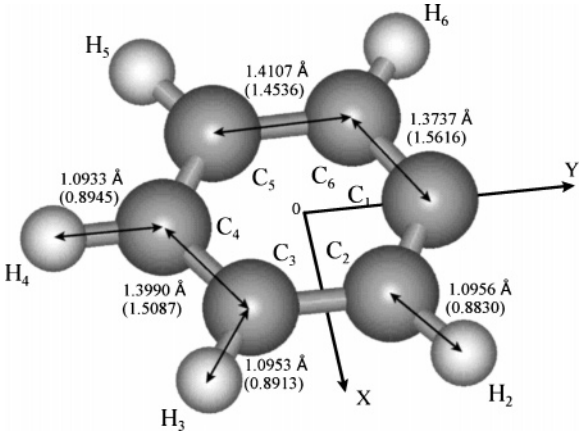

Figure 1. Orientation and atomic numbering of the neutral phenyl radical ($\mathbf{C_6H_5}\bullet$). The C_2,H_2 and C_6,H_6 pairs constitute the *ortho* atoms, while C_3,H_3 and C_5,H_5 are the *meta* pairs. C_4 and H_4 are the *para* carbon and hydrogen atoms, respectively. The figure also lists the relevant bond distances and the bond orders in brackets.

The electronic absorption spectrum of matrix-isolated $\mathbf{C_6H_5}\bullet$ has been determined in the entire 4000−52 000 cm^{-1} region. It consists of three band systems corresponding to transitions

* E-mail: mattar@unb.ca. Telephone: 1 506 447 3091. Fax: 1 506 453 4981.

10.1021/jp065752f CCC: $37.00 © 2007 American Chemical Society
Published on Web 12/19/2006

from its proposed X^2A_1 ground state to three excited electronic states: $^2B_1$(19 589 cm^{-1}), $^2A_1$(42 535 cm^{-1}) and $^2B_2$(47 281 cm^{-1}).[7]

The infrared[8,9] and Raman[10] spectra of $\mathbf{C_6H_5}$•, isolated in argon matrices at ~10 K, have also been determined. Five deuterated isotopomers, $\mathbf{C_6D_5}$•, *para*-$\mathbf{C_6H_4D}$•, *para*-$\mathbf{C_6HD_4}$•, *ortho*-$\mathbf{C_6H_4D}$•, and *meta*-$\mathbf{C_6HD_4}$•, were used to assign the infrared active vibrational modes.[9] The Raman active modes were assigned with the help of the isotopic shifts caused by ^{13}C substitution.[10]

Electron paramagnetic resonance (EPR) and electron−nuclear double resonance (ENDOR) spectroscopies are two of the most powerful tools for studying the net spin density distributions and structure−function relationships of radicals. Even after more than five decades, they still remain the most accurate methods to experimentally determine the nuclear hyperfine (**A**) and gyromagnetic (**g**) tensors of paramagnetic species.[11,12] The first EPR spectrum of $\mathbf{C_6H_5}$•, trapped in various matrices, displayed a triplet of triplets assigned to the hyperfine splittings from its two *ortho* protons, which were further split by the two *meta* protons. However, no splittings due to the *para* proton were observed.[13] Later, Kasai et al.[14] generated the phenyl radical by photolysis of phenyl iodide trapped in an argon matrix at 4 K. From the resulting EPR spectrum, the diagonal **g** tensor elements and some of the five proton **A** tensor components were estimated.[14] This was accomplished by simulating the experimental spectrum as an ensemble of randomly oriented phenyl radicals. The simulations also suggested that the principal axes of the *ortho* and *meta* proton hyperfine tensors did not coincide with those of the **g** tensor.[14]

For the sake of completeness, it is worth mentioning that, in addition to the photolysis of phenyl iodide, $\mathbf{C_6H_5}$• may also be generated by the photodissociation of nitrosobenzene,[15] benzoyl peroxide, and benzoic anhydride in cryogenic matrices.[8] The resulting EPR spectra were found to be identical to those originally generated by Kasai et al.[14]

High-level ab initio and hybrid density functional calculations of the $\mathbf{C_6H_5}$• electronic structure and properties were carried out. They were then compared to some of the experimental and computed spectral parameters. For example, the rotational constants predicted from molecular structure calculations, at the post-Hartree−Fock CCSD(T)/cc-pVTZ level, were found to be in excellent agreement with the experimental measurements.[6] In the case of the infrared spectra, the absorption frequencies were compared with the harmonic frequencies calculated by the UB3LYP hybrid density functional using the cc-pVDZ basis sets. They were found to be within 1% of the gas-phase vibrational frequencies.[9] Similar agreement was obtained for the Raman frequencies when computed by the UB3LYP hybrid density functional and the cc-pVTZ basis sets.[10]

Unlike the infrared and Raman cases, no high-level computations of the **g** and nuclear hyperfine **A** tensor components have been performed. All attempts to calculate the spin Hamiltonian parameters have been limited to the isotropic components, $a^{iso}(^1H)$, of the proton hyperfine tensors using semiempirical methods.[16−18] It was found that the computed $a^{iso}(^1H)$ coupling constants for the *ortho* and *meta* protons are in fair agreement with the experimental values, while the values calculated for the *para* proton are in complete disagreement.[14] This is not surprising, since the $a^{iso}(^1H)$ value is still one of the most difficult molecular properties to compute.[19]

The experimental **g** and **A** tensor components of doublet-state radicals, such as matrix-isolated $\mathbf{C_6H_5}$•, can only be accurately determined by simulating their EPR and ENDOR solid-state spectra.[20] An initial guess for all the unique spin Hamiltonian tensor components must be made to begin the simulation. Since $\mathbf{C_6H_5}$• has C_{2v} symmetry, it can be shown, based purely on symmetry arguments, that none of its eleven nuclei are magnetically equivalent.[21] As a result, each of its five proton Cartesian **A** tensors have different components. It is an overwhelming task to guess that many components in advance. A practical alternative is to compute these **A** and **g** tensor components and then use them as an a priori initial guess in the simulations. These parameters are then iteratively refined until the simulated and experimental spectra match. Therefore, it is very helpful to predict beforehand the numerical values of the **g** and different **A** tensors.

Spatially equivalent atoms in a radical may be magnetically inequivalent because the principal axes of their individual nuclear hyperfine tensors are not aligned with one another. Since these axes represent the interaction between the net electronic spin density and the *local* nuclear spin, they have different orientations for every nucleus. Thus, unlike the **g** tensor, which reflects the overall symmetry of the radical, each hyperfine tensor reflects the unique local site symmetry around its nucleus. The noncoincidence of the principal axes of the spin Hamiltonian tensors, relative to each other, leads to different resonance field positions of the otherwise spatially equivalent atoms.[20,21] This adversely affects their EPR and ENDOR spectra. Thus it is important to know the relative orientation of the principal axes of all the **g** and **A** tensors with respect to one another.

Although there has been considerable effort in computing the isotropic components of **A** tensors,[22] less attention has been given to their anisotropic components and the relative orientation of their principal axes with respect to each other and those of the electronic **g** tensor. Recently, accurate computations of the **g** tensors, using ab initio,[23−26] density functional,[27−31] hybrid density functionals,[32−40] and spectroscopy-oriented configuration interaction,[41] have also become possible. Consequently, one is now in a position to compute, in a reasonable amount of time, the magnitudes of *all* the spin Hamiltonian tensor components and the relative orientations of their principal axes. In turn, the effects of magnetic inequivalency on the EPR and ENDOR spectra may be fully computed and assessed. In this paper, we investigate the magnetic inequivalency of $\mathbf{C_6H_5}$•, based on the computed values and principal axes of its **g** and **A** tensors.

In Section II, the computational details are described. Section IIIA discusses the $\mathbf{C_6H_5}$• electronic structure−bonding relationships. The electronic absorption and vertical excitation spectra, using the spectroscopy-oriented dedicated difference configuration interaction (SORCI) method, are calculated and discussed in Section IIIB. The computed **g** tensor components, by both the coupled-perturbed Kohn−Sham hybrid density functional (CPKS-HDF) and SORCI methods, are discussed in Section IIIC. In addition, its components are broken down into their first- and second-order contributions. They are then analyzed and related to the electronic structure. In the same section, the effects of the hybrid density functional used, the matrix, and the choice of gauge are also investigated. In Section IIID, the experimental and calculated nuclear hyperfine tensors are compared. It is shown that *none* of the in-plane principal axes of the five proton nuclear hyperfine tensor components are the same and are all magnetically inequivalent. The corresponding resonance field positions for the five protons are given, and their magnitudes are estimated from the computed **g** and **A** tensor components. Finally, Section IV summarizes the conclusions of the work performed.

II. Computational Details

The **A** and **g** tensor components were computed by the CPKS-HDF method.[36] The unrestricted forms of the B1LYP and PBE0 hybrid density functionals were used. The calculations were carried out using Neese's ORCA suite of programs[37] on a cluster of eight Linux computers, using the message passing interface protocol (MPICH). In order to make the comparison between the experimental and computed spin Hamiltonian tensors easier, the molecule was oriented in the same way as that of Kasai et al.[14] In a separate set of calculations, the orbital−Zeeman spin−orbit terms of the **g** tensor were also computed by employing the Breit−Pauli spin orbit coupling operator.[38]

There are no structural X-ray data regarding the radical's angles and bond lengths. It was thus imperative to geometry optimize the $\mathbf{C_6H_5}\bullet$ structure. The resulting geometry did not possess any imaginary vibrational frequencies, confirming that it has a global energy minimum.

Barone's EPR-II basis sets[42] were used, and solvent effects were taken into account by surrounding the molecules with a solvent cavity of the appropriate dielectric constant, ϵ, in accordance with the COSMO method.[43,44]

To interpret the experimental ultraviolet−visible (UV−vis) electronic absorption spectrum, determine the vertical excitation energies, and calculate the **g** tensor components using the sum-over-states (SOS) technique, the SORCI method of Neese was employed.[41,45] The next two paragraphs briefly describe the computational details of this new and powerful method. It is a multireference dedicated difference configuration interaction technique[46] used to calculate the energy differences between the states of relatively large molecules.[45]

The initial one-electron molecular orbitals were obtained from a regular HF/EPR-II SCF calculation. The virtual (unoccupied) orbitals were then improved to properly sense an N-1 electron potential.[45] These were then used in an 11-electron−10-orbital complete active space (CAS(11,10)-SCF) calculation to generate an initial CI reference space consisting of 8350 configurations. To reduce this space to a manageable dimension, only the configurations that contribute a weight greater than the value $T_{pre} = 0.0001$ for each root were selected. This produced 165 selected configurations or 336 configuration state functions (CFSs). Single and double excitations from the selected references generated 60 231 210 CFSs. Of these, excitations with a Möller-Plesset second-order perturbation *energy difference* less than $T_{sel} = 10^{-6}$ were discarded, reducing the number of CFSs to 595 789. The Hamiltonian, on the basis of this reference space, was formed and diagonalized to give the required 12 CI roots.

The approximate average natural orbitals (AANOs) were then obtained by diagonalization of a new density matrix formed by averaging the density matrices over all 12 states. To limit the AANOs to a reasonable value, those with a fractional occupation (FO) of less than $T_{nat} = 0.00001$ were not included in later steps. In addition, those with an FO greater than ($2.0T_{nat}$) were frozen. The AANOs are a much improved set compared to the original HF orbitals. Consequently, the procedure used in the previous paragraph was repeated again using the AANOs as the starting orbitals. In both iterative steps, the effects of higher excitations on the energies were included using Davidson's corrections.[45,47] Once completed, the ground-state and transition electron densities were calculated, which, in turn, were used to calculate the electronic excitation energies, transition electric dipole moments, and **g** tensors.

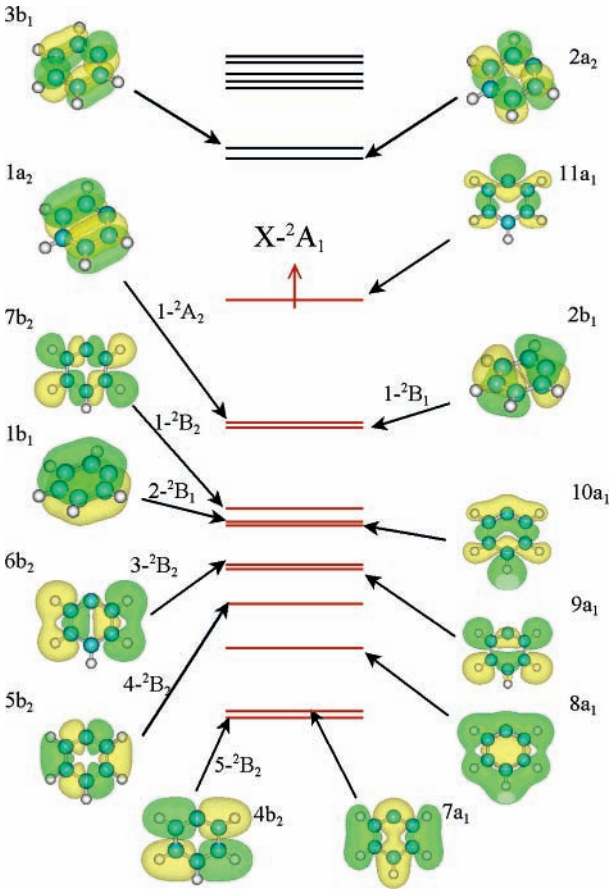

Figure 2. Qualitative one-electron Kohn−Sham molecular orbital diagram of $\mathbf{C_6H_5}\bullet$ in the upper valence region.

III. Results and Discussion

A. Electronic Structure. $\mathbf{C_6H_5}\bullet$ is essentially a benzene molecule that has lost a hydrogen atom (**H•**). As a result of this loss, its symmetry drops from D_{6h} to C_{2v}. Its restricted one-electron Kohn−Sham molecular orbital (MO) diagram, in the upper valence region, is given in Figure 2.

In the case of benzene, the highest occupied molecular orbitals are doubly degenerate and of E_{1g} character. These two E_{1g} orbitals represent out-of-plane π-type combinations and are not affected by the breaking of the σ-type C−H bond. Upon formation of $\mathbf{C_6H_5}\bullet$, they become the $1a_2$ and $2b_1$ orbitals in Figure 2. The benzene E_{2g} orbitals just below the HOMOs are depicted in Figure 3a,b and represent in-plane σ-type interactions. The orbital shown in Figure 3b has a nonbonding pair of C−H bonds. Therefore, it is not largely affected or destabilized by the breaking of one of these two bonds. It becomes the radical's $7b_2$ orbital in Figure 2. In contrast, the orbital of Figure 3a is due to the bonding combinations of *all* the six C−H σ-type bonds. As one of these C−H bonds is broken, it will destabilize. This will cause it to become the highest singly occupied molecular orbital (SOMO), shown as the $11a_1$ orbital in Figure 2.

Thus the HDF calculations strongly suggest that $\mathbf{C_6H_5}\bullet$ has an X^2A_1 ground state with an $7b_2^2,2b_1^2,1a_2^2,11a_1^1$ electronic configuration.

The $\mathbf{C_6H_5}\bullet$ SOMO is depicted in Figure 4. Its Löwdin populations, obtained from a restricted B1LYP/EPR-II calculation, are listed in Table 1. The last column indicates that the unpaired electron is largely C_1 in character (70.5%). It also has a significant amount of *ortho* carbon (16.6%) and hydrogen atoms (3.4%). The *meta* and *para* atoms only constitute a total

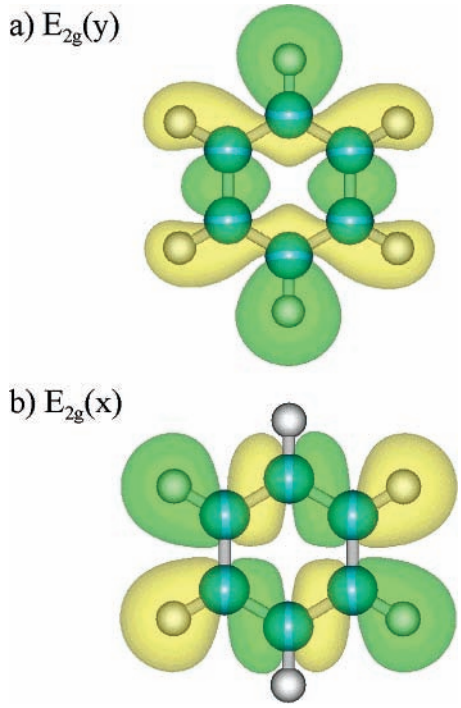

Figure 3. Benzene highest occupied orbitals of E_{2g} symmetry. The degenerate pair is obtained from a restricted B3LYP/EPR-II computation.

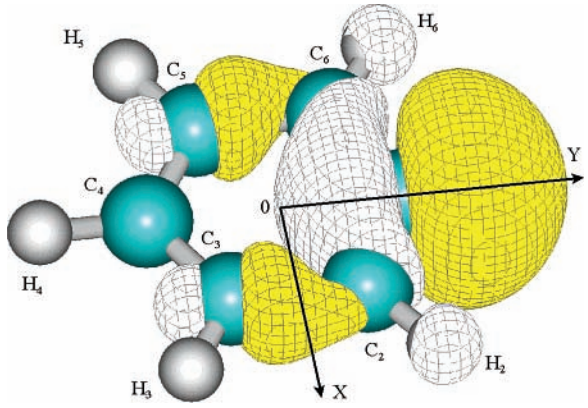

Figure 4. The $C_6H_5\bullet$ three-dimensional isosurface contour plot of its $11a_1$ SOMO.

TABLE 1: Löwdin Reduced Orbital Populations for the SOMO

	S	p_x	p_y	p_z	$d_{x^2-y^2}$	d_{xy}	d_{xz}	d_{yz}	d_{z^2}	total
C_1	9.1	0.0	60.2	0.0	1.0	0.0	0.0	0.0	0.2	70.5
C_2,C_6	0.6	1.5	2.8	0.0	2.5	0.9	0.0	0.0	0.0	16.6
C_3,C_5	0.6	0.0	2.7	0.0	0.0	0.3	0.0	0.0	0.1	3.7
C_4	0.1	0.0	0.0	0.0	0.2	0.0	0.0	0.0	0.0	0.3
H_2,H_6	1.6	0.0	0.1	0.0	0.0	0.0	0.0	0.0	0.0	3.4
H_3,H_5	0.7	0.0	0.1	0.0	0.0	0.0	0.0	0.0	0.0	1.6
H_4	0.2	0.0	0.0	0.0	0.0	0.0	0.0	0.0	0.0	0.2
total	16.4	3.0	71.6	0.0	6.2	2.4	0.0	0.0	0.4	

of 5.8%. The SOMO in Figure 4 has no carbon $2p_z$ character and is formed by the in-plane linear combinations of the 2s(C), $2p_x$(C), $2p_y$(C), and 1s(H) atomic orbitals. The amounts of H_3, H_5, and H_4 s character are 1.4, 1.4, and 0.2%, respectively. They are small enough that they are not apparent in Figure 4. However, the pure s character of H_2 and H_6 is approximately double that of H_3 and H_5 and is sufficiently large to be seen.

TABLE 2: Computed Electronic Excitation Spectra and Transition Dipole Moments Using the SORCI Method[a]

transition	energy	wave-length	T^2	T_x	T_y	T_z
$1^2B_1 - X^2A_1$	23 114	432.6	0.120	0.000	0.000	−0.347
$1^2A_2 - X^2A_1$	29 635	337.4	0.000	0.000	0.000	0.000
$2^2A_1 - X^2A_1$	34 889	286.6	0.000	0.000	0.000	0.000
$1^2B_2 - X^2A_1$	38 689	258.5	0.098	−0.314	0.000	0.000
$2^2A_2 - X^2A_1$	41 895	238.7	0.000	0.000	0.000	0.000
$2^2B_2 - X^2A_1$	42 660	234.4	0.158	0.397	0.000	0.000
$2^2B_1 - X^2A_1$	42 697	234.2	0.293	0.000	0.000	0.541
$3^2A_1 - X^2A_1$	43 358	230.6	0.015	0.000	−0.120	0.000
$3^2B_2 - X^2A_1$	48 704	205.3	0.626	0.791	0.00000	0.000
$3^2B_1 - X^2A_1$	50 155	199.4	0.045	0.000	0.000	−0.211
$4^2A_1 - X^2A_1$	52 225	191.5	0.176	0.000	0.419	0.000

[a] Energies are in cm^{-1}, wavelengths are in nm, and dipole moments are in Debye.

Figure 4 also corroborates that the C_3 and C_5 atomic orbitals are purely p_y in character and form bonding combinations with the s, p_x, and p_y hybrids of the C_2 and C_6 pair respectively. Finally, the large sp hybrid on the C_1 atom (9.1% s and 60.2% p) bonds with respect to both C_2 and C_6.

The computed bond lengths and bond orders are also given in Figure 1. They show that the C−C bond lengths in ascending order are (C_1−C_2, C_1−C_6), (C_5−C_6, C_2−C_3), and (C_3−C_4, C_4−C_5). The bond orders also follow an opposite trend and are, as expected, found to be inversely proportional to the bond lengths. While all five CH bonds are of similar bond orders and lengths, the C−H bonds of the *ortho* protons are the longest, followed by the *meta* bonds, and the *para* C−H bond is the shortest.

B. The Electronic Absorption Spectra. It is inappropriate to estimate the transition energies, transition probabilities, and electronic excitation spectra from the one-electron MO diagram of the HDF calculations. A proper assignment of the transition energies is best accomplished by post-Hartree−Fock techniques, such as multireference configuration interaction computations.

The SORCI method was used to predict the electronic excitation spectra in the 0−55 000 cm^{-1} region. The leading configuration of the X^2A_1 CI ground state (82.61%) is found to be $7b_2^2$, $2b_1^2$,$1a_2^2$,$11a_1^1$. Thus the one-electron DFT picture in Figure 2 and the CI calculations predict a similar electronic structure for the ground state. The remaining minor CI contributions, obtained from the SORCI computations, arise from single and double excitations that lead to electronic configurations such as $7b_2^2$,$2b_1^1$,$1a_2^1$,$11a_1^1$,$2b_1^1$,$1a_2^1$ and $7b_2^2$,$2b_1^2$,$1a_2^0$,$11a_1^1$, $1a_2^2$.

Table 2 lists the computed transition symmetries, energies, and wavelengths. In addition, it includes the *i*th electric transition dipole components:

$$T_x \equiv \langle X^2A_1|ex(B_1)|i\ ^2B_1\rangle,\ T_y \equiv \langle X^2A_1|ey(B_2)|i\ ^2B_2\rangle,\ T_z \equiv \langle X^2A_1|ez(A_1)|i\ ^2A_1\rangle$$

and their corresponding transition probabilities, $T^2 \equiv |\langle X^2A_1|e\vec{r}|i\ ^2A_1\rangle|^2$. In principle, $X^2A_1-{}^2A_2$ transitions are not allowed for a molecule of C_{2v} symmetry. In the standard orientation (where the C_2 axis lies along the *z*-axis and the vertical plane is the *yz* plane), the *x*, *y*, and *z* components of the transition electric dipole moments transform as the B_1, B_2, and A_1 irreducible representations respectively. Their corresponding matrix element

TABLE 3: Experimental and Computed Total g Tensors[a,b]

	g_{xx}	g_{yy}	g_{zz}	$<g>$	g_{xx}	G_{yy}	g_{zz}	$<g>$
experimental[14]	2.0014	2.0023	2.0034	2.00237				
calculated	UB1LP				UBPE0			
				gas phase[c]				
CEC	2.001632	2.002172	2.003030	2.002278	2.001620	2.002169	2.003025	2.002271
CNC	2.001632	2.002172	2.003030	2.002278	2.001620	2.002169	2.003025	2.002271
CNM	2.001633	2.002172	2.003029	2.002278	2.001621	2.002169	2.003024	2.002271
				Ar matrix				
CEC	2.001631	2.002172	2.003039	2.002281	2.001619	2.002170	2.003034	2.002274
CNC	2.001631	2.002172	2.003039	2.002281	2.001619	2.002170	2.003034	2.002274
CNM	2.001632	2.002172	2.003039	2.002281	2.001620	2.002170	2.003033	2.002274
Δg(ppm)	231	128	361	89	219	130	360	96

[a] CEC = center of electronic charge, CNM = center of nuclear mass, and CNC = center of nuclear charge. [b] This article. Due to the C_{2v} symmetry of the $^2A_1$ radical, the total **g** tensor has no off-diagonal components. [c] Gas-phase calculation. No solvent effects are included.

symmetries are the products of the following irreducible representations:

$$\Gamma(A_1) \otimes \Gamma(B_1) \otimes \Gamma(A_2) = \Gamma(B_2)$$

$$\Gamma(A_1) \otimes \Gamma(B_2) \otimes \Gamma(A_2) = \Gamma(B_1) \text{ and}$$

$$\Gamma(A_1) \otimes \Gamma(A_1) \otimes \Gamma(A_2) = \Gamma(A_2)$$

Since they are not equal to the totally symmetrical irreducible representation, $\Gamma(A_1)$, then all three transition dipole moment matrix elements, $\langle X^2A_1|ex\ (B_1)|^2A_2\rangle$, $\langle X^2A_1|ey\ (B_2)|^2A_2\rangle$, and $\langle X^2A_1|ez\ (A_1)|^2A_2\rangle$, are zero. These forbidden transitions may only be weakly allowed via vibronic coupling.

The lowest energy band for $\mathbf{C_6H_5}\bullet$ in an Ar matrix starts at 19 589 cm^{-1}, and its peak maximum occurs around 22 000 cm^{-1}. Previously, this weak band was assigned as the lowest $^2B_1$ $n-\pi$ transition.[7] From Table 2 one observes that, indeed, the lowest energy transition occurs around 231 143 cm^{-1}, which is in good agreement with the experiment. Examination of this $^2B_1$ state shows that its leading configuration (75.59%) is $7b_2^2$, $2b_1^1$, $1a_2^2$, $11a_1^2$, with a 4.65% contribution from the single excitation of the $1b_1$ MO to the $7a_1$ SOMO to give the $1b_1^1$, $7b_2^2$, $2b_1^2$, $1a_2^2$, $11a_1^2$ electronic configuration. It also has a minor contribution (1.18%) from the single excitation of the $11a_1$ electron to the $3b_1$ orbital. Therefore, one can conclude that, qualitatively, the lowest $^2B_1$ transition is indeed $n-\pi$ in nature where an electron has been excited from the ring $2b_1$ π-type orbital, shown in Figure 2, to the $11a_1$ forming a lone pair on the C_1 atom. The next $\mathbf{C_6H_5}\bullet$ band is quite broad and is centered around 42 000 cm^{-1}. It is also relatively weak and has been assigned as the $1^2A_1-X^2A_1$ $\pi-\pi^*$ transition.[7] The calculations in Table 2 show that there are four transitions in this region that may contribute to this broad band. As stated above, the $2^2A_2-X^2A_1$ transition is forbidden and has essentially zero intensity. It will not be considered further. The remaining three transitions, $2^2B_2-X^2A_1$, $2^2B_1-X^2A_1$, and $3^2A_1-X^2A_1$, are very close in energy. The $3^2A_1-X^2A_1$ transition, although weak, has the same symmetry assigned by Radziszewski.[7]

Finally, the third and strongest band occurs around 47 281 cm^{-1} and has B_2 symmetry. This is in very good agreement with the $3^2B_2-X^2A_1$ transition (48 703.6 cm^{-1}), which is also predicted, in Table 2, to have the strongest intensity. Thus the SORCI method, aside from a slight overestimation of the transition energies, seems to be able to properly reproduce the trends in the $\mathbf{C_6H_5}\bullet$ electronic excitation energies.

C. The g Tensor Components. The $\mathbf{C_6H_5}\bullet$ experimental **g** tensor components were first determined by simulation of the X-band EPR spectra at 10 K in an Ar matrix.[14] The simulation program used by Kasai was written before the discovery that field-swept EPR intensities have to be multiplied by the $g_1^p = g_1^2/g$ correction factor rather than g_1^2.[48,49] Therefore, it was worthwhile to re-evaluate the simulated spectra. The new simulations showed insignificant differences in their relative spectral intensities when compared with those of Kasai. This is due to the relatively small **g** tensor anisotropies of this organic radical.

The experimental and calculated **g** tensor components using the CPKS-HDF method at the UB1LYP/EPR-II and UPBE0/EPR-II levels are listed in Table 3. Computations were carried out on $\mathbf{C_6H_5}\bullet$ in the gas phase (GP) and with Ar as the solvent. To study the effects of gauge invariance, the **g** tensor components were also computed with the origin taken as the center of electronic charge (CEC), center of nuclear charge (CNC), and center of nuclear mass (CNM). These results are also listed in Table 3. At the bottom of the table is a row labeled Δg(ppm). It represents the difference between the experimental and computed **g** tensor components, in parts per million. The Δg(ppm) computations used UB1LYP/EPR-II and UPBE0/EPR-II in an Ar matrix and the CEC as the origin.

The **g** tensor principal axes for a radical with C_{2v} symmetry are expected to be aligned with the molecular inertial axes.[50] Consequently, all the off-diagonal **g** tensor components are zero. Indeed this is found to be the case whether the calculations were performed for $\mathbf{C_6H_5}\bullet$ in the GP or in an Ar matrix. Thus only the g_{xx}, g_{yy} and g_{zz} values are listed in Table 3.

The comparison of the **g** tensor components in Table 3 shows that the Ar matrix has no effect on the g_{xx} and g_{yy} components, while the g_{zz} component increases by approximately 3 ppm. Therefore, one concludes that the effects of the Ar matrix are minimal and practically insignificant. Further computations that properly mimic the $\mathbf{C_6H_5}\bullet$ trapped in mono-, di- and tri-vacancies of the solid Ar face-centered-cubic lattice are expected to involve a very large number of Ar atoms. This is presently impractical and beyond the scope of this article.

In general, the experimental **g** tensor components are indirectly determined by the simulation of the EPR spectra of randomly oriented samples such as powders, glassy samples, or matrix-isolated species at low temperatures. Even with these sophisticated simulation programs, their accuracy is expected to be approximately 1 part per thousand or 1000 ppm.[32−34] The $\mathbf{C_6H_5}\bullet$ Δg(ppm) values range from 128 to 361 ppm. Thus the

TABLE 4: Individual One- and Two-Electron Contributions to the Total g Tensor Diagonal Components[a]

	g_{xx}	g_{yy}	g_{zz}	g_{xx}	g_{yy}	g_{zz}
	UB1LP			UBPE0		
$\Delta g^{RMC}\delta_{rs}$	-1.585×10^{-4}	-1.585×10^{-4}	-1.585×10^{-4}	-1.566×10^{-4}	-1.566×10^{-4}	-1.566×10^{-4}
Δg^{GC}_{rs}						
1-elec.	2.708×10^{-4}	7.93×10^{-5}	2.736×10^{-4}	2.725×10^{-4}	7.85×10^{-5}	2.749×10^{-4}
2-elec.	$-1.048 \times\times 10^{-4}$	-3.15×10^{-5}	-1.066×10^{-4}	-1.054×10^{-4}	-3.12×10^{-5}	-1.070×10^{-4}
1 + 2 elec.	1.660×10^{-4}	4.78×10^{-5}	1.670×10^{-4}	1.670×10^{-4}	4.73×10^{-5}	1.679×10^{-4}
$\Delta g^{OZ/SOC}_{rs}$						
1-elec.	-1.529×10^{-3}	-8.87×10^{-5}	1.087×10^{-3}	-1.563×10^{-3}	-9.69×10^{-5}	1.066×10^{-3}
2-elec.	8.333×10^{-4}	5.24×10^{-5}	-3.752×10^{-4}	8.524×10^{-4}	5.66×10^{-5}	-3.631×10^{-4}
1 + 2 elec.	-6.953×10^{-4}	-3.64×10^{-5}	7.113×10^{-4}	-7.103×10^{-4}	-4.03×10^{-5}	7.034×10^{-4}
Δg^{total}_{rs}	-6.878×10^{-4}	-1.471×10^{-4}	7.198×10^{-4}	-6.998×10^{-4}	-1.496×10^{-4}	7.147×10^{-4}
$g_e + \Delta g^{total}_{rs}$	2.001631	2.002172	2.003039	2.001619	2.002170	2.003034

[a] The molecular symmetry axes coincide with the **g** tensor principal axes.

calculated **g** tensor is in excellent agreement with the experiment and well within the limits of experimental accuracy. In addition, when comparing the UB1LYP and UPBE0 methods, the maximum differences in Δg(ppm) are only 12, 2, 1, and 7 ppm for g_{xx}, g_{yy}, g_{zz}, and $<g>$, respectively. Therefore, both HDF methods yield similar results and are quite accurate. This is understandable since both the UB1LYP and UPBE0 functionals are similar and mix 25% of the HF exchange with 75% of the density functional.[51,22]

One possible drawback of the calculated **g** tensor is that it is not gauge invariant. However, if moderate or large basis sets are used, its effect is greatly reduced. The gauge dependency of the **g** tensor components when calculated with Barone's EPR-II basis sets have been tested. Inspection of Table 3 shows that, whether the origin is chosen as the CEC, CNC, or CNM, the difference is at most ±1 ppm. Thus the gauge invariance of the **g** tensor does not pose a problem in this case.

The **g** tensor components are made up of four main terms given by

$$g_{pq} = g_e\delta_{pq} + \Delta g^{RMC}\delta_{pq} + \Delta g^{GC}_{pq} + \Delta g^{OZ/SOC}_{pq} \qquad (1)$$

Their computed values using the UB1LYP/EPR-II and UPBE0/EPR-II methods in an Ar matrix are listed in Table 4, and all the symbols appearing in eqs 1−4 have been previously defined.[36,32,33] Both HDF techniques give very similar results. For the sake of brevity, we will concentrate on the UB1LYP/EPR-II values. The first term is the free electron value, $g_e = 2.002319$, and the δ_{pq} Kronecker delta function limits its contribution to the diagonal components of the total **g** tensor. The relativistic mass correction to the kinetic energy is[36]

$$\Delta g^{RMC} = \left(-\frac{\alpha^2}{S}\cdot\frac{g_e}{2}\right)\sum_{\mu,\nu} P^{\alpha-\beta}_{\mu\nu}\left\langle\psi_\mu\left|\frac{-\vec{\nabla}^2}{2}\right|\psi_\nu\right\rangle \qquad (2)$$

where the spin is $S = 1/2$, α is the fine structure constant, and $P^{\alpha-\beta}_{\mu\nu}$is the net spin density. The Δg^{RMC} term decreases the diagonal **g** tensor values by 1.585×10^{-4}.

In contrast to the first two terms, the diamagnetic correction term, Δg^{GC}_{pq}, is a second-rank Cartesian tensor:[36]

$$\Delta g^{GC}_{pq} = \frac{1}{2S}\sum_{\mu,\nu} P^{\alpha-\beta}_{\mu\nu}\langle\psi_\mu|\sum_A \xi(r_A)[\vec{r}_A\vec{r} - \vec{r}_{A,p}\vec{r}_q]|\psi_\nu\rangle \qquad (3)$$

The term $\xi(r_A)$ is the effective spin orbit coupling interaction at the Ath nucleus. Table 4 shows that the one-electron contributions to Δg^{GC}_{xx}, Δg^{GC}_{yy}, and Δg^{GC}_{zz} are positive, while the corresponding two-electron terms are approximately half the one-electron terms and negative. This produces positive Δg^{GC}_{xx}, Δg^{GC}_{yy}, and Δg^{GC}_{zz} values that counteract the corresponding Δg^{RMC} contributions.

The orbital−Zeeman spin−orbit term $\Delta g^{OZ/SOC}_{pq}$ is the largest contributing term to the deviation of the **g** tensor from the free electron value.[36] When the effective one-electron spin−orbit operator is expressed as an accurate mean-field approximation to the full Breit−Pauli spin−orbit coupling operator, it takes the form[38]

$$\Delta g^{OZ/SOC}_{pq} = -\frac{1}{2S}\sum_{\mu,\nu}\frac{\partial P^{\alpha-\beta}_{\mu\nu}}{\partial B_p}\left\{\langle\varphi_\mu|\hat{h}^{1el-SOC}_p|\varphi_\nu\rangle + \sum_{\kappa\tau} P^{(\alpha+\beta)}_{\kappa\tau}\left[\langle\varphi_\mu\varphi_\nu|\hat{g}^{SSO}_p|\varphi_\kappa\varphi_\tau\rangle - \frac{3}{2}\langle\varphi_\mu\varphi_\kappa|\hat{g}^{SOC}_p|\varphi_\tau\varphi_\nu\rangle - \frac{3}{2}\langle\varphi_\tau\varphi_\nu|\hat{g}^{SOC}_p|\varphi_\mu\varphi_\kappa\rangle\right]\right\} \qquad (4)$$

where B_p is the pth component of the magnetic field. Here, $P^{(\alpha+\beta)}_{\kappa\tau}$is the total charge density matrix,

$$\hat{h}^{1el-SOC}_p(\vec{r}_i) = \frac{\alpha^2}{2}\sum_A \frac{Z_A \hat{l}_{iA;p}}{\vec{r}_i^{\,3}} \qquad (5)$$

is the one-electron spin−orbit coupling operator, $\hat{l}_{iA;p}$ is the pth component of the angular momentum of electron i relative to nucleus A, and

$$\hat{g}^{SOC}_p(\vec{r}_i,\vec{r}_j) = \frac{\alpha^2}{2}\frac{\mathbf{l}_{ij;p}}{\vec{r}_{ij}^{\,3}} \qquad (6)$$

is the corresponding two-electron operator. Similarly, $\hat{l}_{ij;p}$ is the pth component of the ith electron angular momentum relative to electron j.

Only the coupling of the $^2A_1$ ground state with the excited $^2B_1$ states contributes to the $\Delta g^{OZ/SOC}_{xx}$ components. Positive contributions to g_{xx} arise from the excitation of the $1b_1$ and $2b_1$ electrons to the $11a_1$ SOMO shown in Figure 2. However a counteracting negative contribution to g_{xx}, in the region of 0−50 000 cm^{-1}, stems mainly from the excitation of the $11a_1$ electron to the $3b_1$ empty orbital. The net result is $\Delta g^{OZ/SOC}_{xx} = -6.953 \times 10^{-4}$, as shown in Table 4.

Spin−orbit couplings between the X^2A_1 ground state and excited states of A_2 symmetry will affect the $g^{OZ/SOC}_{yy}$. There are two predominant excitations to take into consideration. The first

TABLE 5: Computed Contributions to the Total g Tensor with the SORCI Method

	g_{xx}	g_{yy}	g_{zz}
$\Delta g^{RMC}\delta_{rs}$ tot.	-1.503×10^{-4}	-1.503×10^{-4}	-1.503×10^{-4}
Δg_{rs}^{GC} tot.	1.338×10^{-4}	1.810×10^{-5}	1.273×10^{-4}
$\Delta g_{rs}^{OZ/SOC}$ tot.	-1.574×10^{-4}	1.32×10^{-5}	-6.000×10^{-7}
transition	$\Delta g_{xx}^{OZ/SOC}$	$\Delta g_{yy}^{OZ/SOC}$	$\Delta g_{zz}^{OZ/SOC}$
$1^2B_1 - X^2A_1$	2.184×10^{-4}	0.0000	0.0000
$1^2A_1 - X^2A_1$	0.0000	2.000×10^{-4}	0.0000
$2^2A_1 - X^2A_1$	0.0000	0.0000	0.0000
$1^2B_1 - X^2A_1$	0.0000	0.0000	-5.000×10^{-7}
$2^2A_1 - X^2A_1$	0.0000	1.110×10^{-5}	0.0000
$2^2B_1 - X^2A_1$	0.0000	0.0000	0.0000
$2^2B_1 - X^2A_1$	-4.275×10^{-4}	0.0000	0.0000
$3^2A_1 - X^2A_1$	0.0000	0.0000	0.0000
$3^2B_1 - X^2A_1$	0.0000	0.0000	0.0000
$3^2B_1 - X^2A_1$	5.17×10^{-5}	0.0000	0.0000
$4^2A_1 - X^2A_1$	0.0000	0.0000	0.0000
Δg_{rs} tot.	-1.738×10^{-4}	-1.190×10^{-4}	-2.350×10^{-5}
$g_e + \Delta g_{rs}$ tot.	2.002145	2.002200	2.002296

is the excitation of an electron from the $1a_2$ orbital to the $11a_1$ SOMO, while the second is the excitation of the $11a_1$ unpaired electron to the $2a_2$ empty orbital. These oppose one another, leading to a small $\Delta g_{yy}^{OZ/SOC}$ of -3.64×10^{-5}. The $^2B_2-X^2A_1$ transitions in the same energy range also influence $\Delta g_{zz}^{OZ/SOC}$. These excitations stem from the coupling of the $5b_2$, $6b_2$, and $7b_2$ to the half-filled $11a_1$ orbital. This results in a relatively large and positive value for $\Delta g_{zz}^{OZ/SOC}$ of 7.113×10^{-4}.

In summary, the **g** tensor components computed by the CPKS-HDF method are in excellent agreement with the experiment.

The **g** tensor components were also computed using the SORCI method. The same excitation energy differences, $E_b - E_0$, used in the calculation of the UV−vis spectra of Section IIIB were used in conjunction with the SOS procedure. In this case,

$$\Delta g_{pq}^{OZ/SOC} = -\frac{1}{2S}\sum_b \frac{1}{E_b - E_0}\{\sum_{\mu\nu} P_{\mu\nu}^{(\alpha+\beta),0b} \langle\psi_\mu|l_p|\psi_\nu\rangle \sum_{\mu\nu} P_{\mu\beta}^{(\alpha-\beta),b0} \langle\psi_\mu|\sum_A \xi(\vec{r}_A) l_{A,q}|\psi_\nu\rangle + \sum_{\mu\nu} P_{\mu\nu}^{(\alpha-\beta),0b} \langle\psi_\mu|\sum_A \xi(\vec{r}_A) l_{A,p}|\psi_\nu\rangle \sum_{\mu\nu} P_{\mu\nu}^{(\alpha+\beta),b0} \langle\psi_\mu|l_q|\psi_\nu\rangle\} \quad (7)$$

is used instead of eq 4. Here $P_{\mu\nu}^{(\alpha+\beta),0b}$ and $P_{\mu\nu}^{(\alpha-\beta),0b}$are the total charge and net spin transition density matrices between the 0 and *b* states.[41]

Table 5 shows that Δg^{RMC} computed by the SORCI method is 1.503×10^{-4} and is slightly less than the corresponding 1.585×10^{-4} obtained by the CPKS-HDF technique. Similarly, the Δg_{pq}^{GC} values from Tables 4 and 5 indicate that those obtained by the SORCI method are also marginally less than their CPKS-HDF counterparts. On the other hand, the SOS and CPKS-HDF $\Delta g_{pq}^{OZ/SOC}$ values are quite different. Their $\Delta g_{yy}^{OZ/SOC}$and $\Delta g_{zz}^{OZ/SOC}$ even differ in sign. The total g_{xx}, g_{yy}, and g_{zz} tensor components, obtained by the SOS method, differ from the experimental ones by −745, 100, and 1104 ppm, respectively. Although this is considered to be acceptable, they are clearly inferior to those obtained by the CPKS-HDF method. A probable explanation of the poorer performance of the SOS technique is an insufficient number of roots (states) that contribute to eq 7. Increasing the number of roots from the present case of 12 may improve the situation. However, there is a limit to such a remedy, since computations using a larger number of roots may become prohibitively expensive for multireference configuration interaction techniques, even if they are specially tailored to be efficient, such as the SORCI program. This is definitely a drawback for the SOS procedure and gives an edge to the methods that use derivatives, such as the CPKS-HDF. Finally, for the sake of completeness, the transition energies, spin−orbit coupling, and orbital−Zeeman matrix elements needed in eq 7 are listed in Table 6.

D. The Nuclear Hyperfine Tensor Components. The nine Cartesian nuclear hyperfine tensor components, $A_{pq}(N)$ for a nucleus *N*, may be broken down into three components:

$$A_{pq}(N) = a^{iso}(N)\,\delta_{pq} + A_{pq}^{dip}(N) + A_{pq}^{SOC}(N) \quad (8)$$

The first is the isotropic Fermi contact term,

$$a^{iso}(N) = \frac{4\pi}{3}\left(\frac{1}{S}\right) g_e\beta_e g_N\beta_N \rho(\vec{R}_N) \quad (9)$$

where $\rho(\vec{R}_N)$ is the net electron spin density matrix at the nuclear position, $\vec{R}_N$.[52] The second is the magnetic dipole−dipole interaction between the electron and the nucleus:[53]

$$A_{pq}^{dip}(N) = g_e\beta_e g_N\beta_N \sum_{kl} P_{kl}^{\alpha-\beta} \left\langle \varphi_k \left| \frac{3\vec{r}_{Np}\vec{r}_{Nq} - \delta_{pq}\vec{r}_N^2}{\vec{r}_N^5} \right| \varphi_l \right\rangle \quad (10)$$

Here the vector $\vec{r}_N$ points from nucleus *N* to the electron. Both these terms may be calculated using regular HDF techniques. The last term, $A_{pq}^{SOC}(N)$, in eq 8 is due to second-order spin−orbit coupling. It may be determined by using the CPKS-HDF method.[36] Due to the small spin−orbit coupling constants of H and C, the $A_{pq}^{SOC}(N)$ components were found to be less than 0.1 MHz. Therefore, they will not be considered in the following discussion.

C_6H_5• is a σ−type radical. Therefore, its SOMO, shown in Figure 4, has no nodal plane, and its isotropic hydrogen hyperfine coupling constants, $a^{iso}(^1H)$, unlike out-of-plane π-type radicals, are due to both "s" spin density and core polarization at their nuclei. Their values, computed at the UB1LYP/EPR-II level, are $a^{iso}(^1H_2) = a^{iso}(^1H_6) = 17.794$ G, $a^{iso}(^1H_3) = a^{iso}(^1H_5) = -5.935$ G, and $a^{iso}(^1H_4) = 2.194$ G. This is because H_2 and H_6 form the *spatially equivalent ortho* pair, while H_3 and H_5 are the *spatially equivalent meta* pair. Unfortunately, one cannot directly determine the isotropic hyperfine constants or their signs from a matrix-isolation EPR spectrum alone. However, a good estimate may be obtained from the experimental total hyperfine components as

$$a^{iso}(N) = \frac{A_{xx}(N) + A_{yy}(N) + A_{zz}(N)}{3} \quad (11)$$

Their absolute experimental values, estimated from Table 7 and eq 11, are $a^{iso}(^1H_2) = a^{iso}(^1H_6) = 17.40$ G, $a^{iso}(^1H_3) = a^{iso}(^1H_5) = 5.90$ G, and $a^{iso}(^1H_4) = 1.90$ G.[14] This is in excellent agreement with the computed values listed above. The maximum deviation between the calculated and experimental values is only 0.39 G and occurs for $a^{iso}(^1H_2)$ and $a^{iso}(^1H_6)$.

The matrix isolation experiments do not allow us to predict the radical's equilibrium geometry, bond lengths, and angles. However, the isotropic hyperfine coupling constants are extremely sensitive to the radical's geometry. The excellent agreement between theory and experiment obtained here is a strong indication that the optimized geometry, at the UB1LYP/EPR-II level, is very close to the true geometry in the matrix.

The calculated and experimental ^1H total hyperfine tensor components are given in Table 7. From this table, it is seen

TABLE 6: Computed Orbital−Zeeman and Spin−Orbit Coupling Terms Using the SORCI Method[a,b]

transition	ΔE	l_x	l_y	l_z	$(SOC)_x$	$(SOC)_y$	$(SOC)_z$
$1^2B_1 - X^2A_1$	23 114.3	−0.3891	0.0000	0.0000	6.4870	0.0000	0.0000
$1^2A_2 - X^2A_1$	29 635.1	0.0000	−0.0072	0.0000	0.0000	4.228	0.0000
$2^2A_1 - X^2A_1$	34 889.9	0.0000	0.0000	0.0000	0.0000	0.0000	0.0000
$1^2B_2 - X^2A_1$	38 689.4	0.0000	0.0000	0.0855	0.0000	0.0000	0.1220
$2^2A_2 - X^2A_1$	41 895.9	0.0000	0.0619	0.0000	0.0000	−3.768	0.0000
$2^2B_2 - X^2A_1$	42 660.3	0.0000	0.0000	−0.0001	0.0000	0.0000	0.0820
$2^2B_1 - X^2A_1$	42 697.0	−0.5667	0.0000	0.0000	−16.105	0.0000	0.0000
$3^2A_1 - X^2A_1$	43 358.4	0.0000	0.0000	0.0000	0.0000	0.0000	0.0000
$3^2B_2 - X^2A_1$	48 703.6	0.0000	0.0000	−0.1324	0.0000	0.0000	−0.0040
$3^2B_1 - X^2A_1$	50 154.5	−0.1709	0.0000	0.0000	7.5850	0.0000	0.0000
$4^2A_1 - X^2A_1$	52 225.4	0.0000	0.0000	0.0000	0.0000	0.0000	0.0000

[a] Transition energies, ΔE, and spin−orbit coupling components, $(SOC)_{x,y,z}$, are given in cm^{-1}. [b] Orbital−Zeeman terms, l_x,l_y, and l_z, are listed in a.u.

TABLE 7: Calculated Total ^1H Hyperfine Tensor Components[a,b,c]

$A(^1H_4)$	x	y	z	exp.	x	y	z
x	2.528	0.0	0.0	x	2.5	0.0	0.0
y	0.0	2.415	0.0	y	0.0	2.0	0.0
z	0.0	0.0	1.64	z	0.0	0.0	1.2
α	0.0			α	0.0		
$A(^1H_2, ^1H_6)$	x	y	z	exp.	x	y	z
x	16.039	±1.231	0.0	x	15.5	±0.84	0.0
y	±1.231	21.900	0.0	y	±0.84	21.9	0.0
z	0.0	0.0	15.450	z	0.0	0.0	14.9
α	±11.39			α	±7.5		
$A(^1H_3, ^1H_5)$	x	y	z	exp.	x	y	z
x	6.234	±1.187	0.0	x	6.31	±0.25	0.0
y	±1.187	6.704	0.0	y	±0.25	6.35	0.0
z	0.0	0.0	4.867	z	0.0	0.0	5.0
α[a]	±40.2				±40.0		

[a] Values in Gauss (G). [b] The signs of the hyperfine tensor components were not experimentally determined. [c] The angle α is the deviation of the in-plane principal axes from the x and y molecular symmetry axes.

that the *para* hydrogen nuclear hyperfine tensor has no off-diagonal tensor components. This is because $\mathbf{C_6H_5}$• has C_{2v} symmetry, and the $^1H_4$ proton lies along its C_2 main symmetry axis. This also causes the $A(^1H_4)$ principal tensor axes to be collinear with the molecular symmetry axes. Since the **g** tensor principal axes also coincide with the molecular symmetry axes, then the angle α in Table 7 for this proton is 0.0. In addition, the $A(^1H_4)$ diagonal components are not equal or $A_{xx}(^1H_4) \neq A_{yy}(^1H_4) \neq A_{zz}(^1H_4) \neq 0$. This is a direct consequence of the absence of doubly degenerate irreducible representations in radical's C_{2v} molecular symmetry point group.

The $A_{pq}^{dip}(^1H_4)$ have also been calculated and are: $A_{xx}^{dip}(^1H_4) = 0.333$ G, $A_{yy}^{dip}(^1H_4) = 0.221$ G and $A_{zz}^{dip}(^1H_4) = -0.554$ G. As expected, their sum is zero since, by definition, the dipole−dipole hyperfine tensor is traceless. One also notes that, because of the negligible contribution of $A_{pq}^{SOC}(^1H_4)$ then $A_{pq}(^1H_4) \approx a^{iso}(^1H_4)\ \delta_{pq} + A_{pq}^{dip}(^1H_4)$. Table 7 also shows that there is excellent agreement between the calculated and experimental $\mathbf{A}(^1H_4)$ tensor components. In the worst case, the difference between the experimental and computed values is 0.415 G.

Although $\mathbf{C_6H_5}$• contains two *ortho* and two *meta* hydrogen atoms that are spatially equivalent, none can be totally or magnetically equivalent because the radical has C_{2v} symmetry.[21] Pairs of spatially equivalent atoms, such as the *ortho* or *meta* hydrogens, have the same isotropic hyperfine coupling constants, but their total hyperfine tensor components and directions of their principal axes are not the same. This causes them to have different resonance field positions.[20,21,50,54−56] If these differences are larger than the EPR natural line widths, then extra lines are expected to be resolved and observed. In contrast, if they are less than the line widths, then they may appear as shoulders or inhomogeneously broadened resonances.

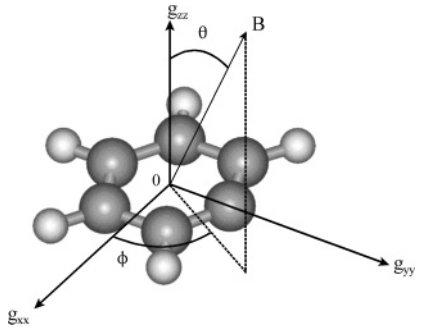

Figure 5. Angles θ and φ that define the external homogeneous magnetic field, B, with respect to the $\mathbf{C_6H_5}$• molecular and the g tensor principal axes.

The $\mathbf{A}(^1H_2)$ and $\mathbf{A}(^1H_6)$ values are listed in Table 7. The original experimental values given by Kasai et al.[14] lie along the principal axes of the **g** tensor. The corresponding ones listed in Table 7 are obtained from Kasai's values after rotating them, via an $R^{\dagger}AR$ similarity transformation, by the specified angle, α. The rotation matrix takes the form

$$R = \begin{pmatrix} \cos(\alpha) & -\sin(\alpha) & 0 \\ \sin(\alpha) & \cos(\alpha) & 0 \\ 0 & 0 & 1 \end{pmatrix} \quad (12)$$

Table 7 shows that the computed $\mathbf{A}(^1H_2)$ and $\mathbf{A}(^1H_6)$ values are anisotropic and contain off-diagonal elements in the xy plane. $A_{xy}(^1H_2) = A_{yx}(^1H_2) = 1.231$ G, while the corresponding $A_{xy}(^1H_6) = A_{yx}(^1H_6) = -1.231$ G. One also notes that the $A(^1H_2)$ and $A(^1H_6)$ principal axes deviate from the molecular and **g** tensor axes by 11.4° and −11.4°, respectively. The differences in sign and angles between the H_2 and H_6 of diagonal elements causes their corresponding resonance field positions, $B(H_2)$ and $B(H_6)$, to also be different, which leads to magnetic inequivalency. This was first recognized by Kasai, and provisions had to be made to properly simulate the experimental $\mathbf{C_6H_5}$• EPR spectra.[14] The resonance field positions for H_2 and H_6 are[56]

$$B(^1H_j) = -\frac{m_I}{g^2\beta}\{A_{zz}^2(^1H_j)\, g_{zz}^2 \cos^2\theta + [A_{xx}(^1H_j)\, g_{xx}\cos\varphi + A_{yx}(^1H_j)\, g_{yy}\sin\varphi]^2 \sin^2\theta + [A_{yy}(^1H_j)\, g_{yy}\sin\varphi + A_{yx}(^1H_j)\, g_{xx}\cos\varphi]^2 \sin^2\theta\}^{(1/2)} \quad (13)$$

where $j = 2,6$. The angles θ and φ are defined in Figure 5, and the expression for the effective g value appearing in eq 13 in terms of its components is[56]

$$g = \sqrt{g_{xx}^2\cos^2\theta + [g_{zz}^2\cos^2\varphi + g_{yy}^2\sin^2\varphi]\sin^2\theta} \quad (14)$$

Thus, to estimate the resonance field positions, one needs to calculate *all* the nuclear hyperfine *and* **g** tensor components.

To illustrate the effects of magnetic inequivalency and the nonalignment of the nuclear hyperfine principal axes on the matrix-isolated $\mathbf{C_6H_5}$• EPR spectra, the H_2 and H_6 proton pair are taken as an example. Their EPR line shapes were simulated as a function of α and displayed in Figure 6. The simulation parameters used were identical to the experimental ones determined by Kasai.[14] The angle α is defined as the angle made by the A_{xx} principal axis of the *ortho* H_2 proton and the g_{xx} principal axis. To unclutter and simplify the resulting spectra, the hyperfine interactions arising from the H_3, H_4, and H_5 protons were suppressed. In accordance with eq 13, Figure 6 shows that, as α is increased from 0 to 50°, shifts as large as 7.0 G in the resonance field positions occur, which in turn lead to dramatic changes in the overall line shapes. It is also worth noting from Table 7 that the experimental and computed $\mathbf{A}(^1H_2)$ and $\mathbf{A}(^1H_6)$ tensor components are in very good agreement, and the maximum differences between them are less than 1.0 G.

Similar effects are also found for the H_3 and H_5 proton pair. In this case, the deviation of their in-plane principal axes from those of the **g** tensor are ±40°, respectively. These angles are almost identical to those determined experimentally. Finally the agreement between all the calculated and experimental $\mathbf{A}(^1H_3)$ and $\mathbf{A}(^1H_5)$ tensor components is just as good as that of the $\mathbf{A}(^1H_2)$ and $\mathbf{A}(^1H_6)$ pair. Thus one can safely conclude that the B1LYP/EPR-II HDF method can accurately reproduce the magnitudes of the $\mathbf{C_6H_5}$• proton hyperfine tensor components and the relative orientations of their principal axes.

The inequivalency of the (H_2,H_6) and (H_3,H_5) pairs is particularly significant since the hydrogen atoms only have s-character. The anisotropy required to misalign their in-plane nuclear hyperfine principal axes relative to those of the **g** tensor is induced indirectly from the adjacent $2p_x(C_2)$, $2p_y(C_2)$, $2p_x(C_6)$, $2p_y(C_6)$, $2p_x(C_3)$, $2p_y(C_3)$, $2p_x(C_5)$, and $2p_y(C_5)$ involved in the formation of the four C−H σ bonds.

Although the simulations were carried out using a special program written in our laboratory,[54] readily available programs, such as the shareware version of SIMFONIA by Bruker BioSpin, yield identical results. They may be used, in this and similar cases, to probe the effects of magnetic inequivalency.

The calculated ^{13}C total hyperfine tensor components are listed in Table 8. Unfortunately however, they were not resolved in the EPR spectra and were not determined experimentally. An ENDOR spectrum of the matrix-isolated $\mathbf{C_6H_5}$• may have enough resolution to show the ^{13}C powder hyperfine patterns. Until such time, no comparison with experiment can be undertaken.

IV. Summary and Conclusions

Electronic structure calculations using HDF techniques indicate that the matrix-isolated $\mathbf{C_6H_5}$• radical has an X^2A_1 ground state due to the $7b_2^2$, $2b_1^2$, $1a_2^2$, $11a_1^1$ electronic configuration. The $11a_1$ SOMO has in-plane σ bonding with no out-of-plane π bonding. It is mainly an sp_y hybrid on the C_1 atom (9.1% s and 60.2% p_y). It also has a significant amount of *ortho* carbon and hydrogen character due to the bonding of the C_1 sp_y hybrid with both the C_2 and C_6 atoms.

The SORCI method was also used to predict the electronic structure. The leading configuration of the X^2A_1 CI ground state is also found to be predominantly (82.61%) $7b_2^2$, $2b_1^2$, $1a_2^2$, $11a_1^1$. Therefore the HDF and SORCI calculations predict a similar electronic structure for the $\mathbf{C_6H_5}$• ground state.

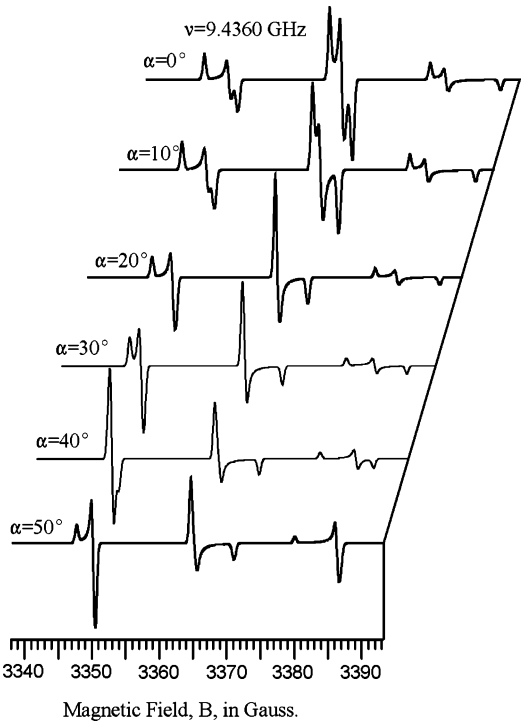

Figure 6. The simulated EPR spectrum of matrix-isolated $\mathbf{C_6H_5}$• as a function of α, defined as the angle made by the A_{xx} principal axis of the *ortho* H_2 proton and the g_{xx} principal axis. For clarity, only the hyperfine interactions from the *ortho* H_2 and H_6 protons were simulated. Simulation parameters are microwave frequency = 9.4360 GHz, g_{xx} = 2.0014, g_{yy} = 2.0023, g_{zz} = 2.0034, A_{xx} = 21.9, A_{yy} = 15.4, A_{zz} = 14.9 G, and Gaussian line widths: $\Delta B_{xx} = \Delta B_{yy} = \Delta B_{zz}$ = 0.5 G.

TABLE 8: Calculated Total ^{13}C Hyperfine Tensor Components

$A(^{13}C_1)$	x	y	z	$A(^{13}C_4)$	x	y	z
x	186.582	0.0	0.0	x	−1.253	0.0	0.0
y	0.0	114.662	0.0	y	0.0	−1.874	0.0
z	0.0	0.0	121.1565	z	0.0	0.0	−5.200
α	0.0			α	0.0		
$A(^{13}C_2)$	x	y	z	$A(^{13}C_6)$	x	y	z
x	7.352	−3.075	0.0	x	7.352	3.075	0.0
y	−3.075	7.888	0.0	y	3.075	7.888	0.0
z	0.0	0.0	0.225	z	0.0	0.0	0.225
α	−42.5			α	42.5		
$A(^{13}C_3)$	x	y	z	$A(^{13}C_5)$	x	y	z
x	19.488	−0.281	0.0	x	19.488	0.281	0.0
y	−0.281	14.923	0.0	y	0.281	14.923	0.0
z	0.0	0.0	16.793	z	0.0	0.0	16.793
α	−3.53			α	3.53		

The $\mathbf{C_6H_5}$• electronic excitation spectrum, in the range of 0−50 000 cm^{-1}, was predicted by the SORCI method. The method slightly overestimates the transition energies, but properly reproduces their trends.

The **g** tensor components, computed by the CPKS-HDF method, are found to be in excellent agreement with experiment. In addition, the calculations show that the Ar matrix has practically no effect on the **g** tensor components (less than 3 ppm). When the EPR-II basis set is used, the gauge invariance of the **g** tensor does not play a significant role. The variations in the tensor components are less than ±1 ppm whether the origin is chosen as the CEC, CNC, or CNM.

The proton hyperfine tensor components were calculated by the B1LYP and PBE0 functionals. The computed isotropic

hyperfine components were in excellent agreement with those obtained from the absolute experimental values by averaging their diagonal components. As expected, the a^{iso} values for the spatially equivalent (H_2,H_6) and (H_3,H_5) pairs were found to be equal. Due to the high dependence of the a^{iso} values on the molecular geometry, the very good agreement between theory and experiment suggests that the optimized geometry is very close to the true geometry in the matrix.

The $\mathbf{A}(^1H_4)$ tensor is diagonal, and there is an excellent match between its calculated and experimental components. The maximum difference between the experimental and computed values is 0.415 G.

The *ortho* $\mathbf{A}(^1H_2)$, $\mathbf{A}(^1H_6)$ and *meta* $\mathbf{A}(^1H_3)$, $\mathbf{A}(^1H_5)$ tensors are anisotropic and contain off-diagonal elements in the *xy* plane. The differences in sign between the (H_2, H_6) and (H_3, H_5) off-diagonal elements causes their principal axes and corresponding resonance field positions be different. Thus, although *ortho* H_2 and H_6 are spatially equivalent, they are not magnetically equivalent. A similar reasoning also applies to the *meta* H_3, H_5 pair.

The computed *ortho* and *meta* proton hyperfine tensor components are very similar to the experimental values. The maximum differences between them are less than 1.0 G. In addition, the deviations of their in-plane principal axes from those of the **g** tensor are almost identical to those determined by experiment. Thus, one can safely conclude that the B1LYP/EPR-II HDF method can accurately reproduce the magnitudes of the $\mathbf{C_6H_5}$• proton hyperfine tensor components and the relative orientations of their principal axes.

To the best of our knowledge, the $\mathbf{C_6H_5}$• is the first aromatic in-plane σ-type radical whose **g** and **A** tensor anisotropies are computed and used to completely predict the magnetic in-equivalency and difference in the resonance field positions of spatially equivalent but magnetically inequivalent atoms.

Acknowledgment. This article is dedicated to Dr. Paul H. Kasai for his long and outstanding contribution to the field of EPR of matrix-isolated species. I thank the Natural Sciences and Engineering Research Council of Canada for financial support in the form of Discovery (Operating) grants. I am also grateful to Professor Frank Neese for the use of his ORCA suite of programs.

References and Notes

(1) Haynes, D. S. *Fossil Fuel Combustion*; Wiley-Interscience: New York, 1991; p 261.
(2) Bockhorn, H. *Soot Formation in Combustion*; Springer: New York, 1993.
(3) Harspool, W. M. *CRC Handbook of Organic Photochemistry and Photobiology*; CRC Press: Boca Raton, FL, 1995.
(4) Herbst, E. *Annu. Rev. Phys. Chem.* **1995**, *46*, 27.
(5) Woods, P. M.; Millar, T. J.; Zijlstra, A. A.; Herbst, E. *Astrophys. J.* **2002**, *574*, L167.
(6) McMahon, R. J.; McCarthy, M. C.; Gottlieb, C. A.; Dudek, J. B.; Stanton, J. F.; Thaddeus, P. *Astrophys. J.* **2003**, *590*, L167.
(7) Radziszewski, J. G. *Chem. Phys. Lett.* **1999**, *301*, 565.
(8) Radziszewski, J. G.; Nimlos, M. R.; Winter, P. R.; Ellison, G. B. *J. Am. Chem. Soc.* **1996**, *118*, 7400.
(9) Friderichsen, A. V.; Radziszewski, J. G.; Nimlos, M. R.; Winter, P. R.; Dayton, D. C.; David, D. E.; Ellison, G. B. *J. Am. Chem. Soc.* **2001**, *123*, 1977.
(10) Lapinski, A.; Spanget-Larsen, J.; Langgard, M.; Waluk, J.; Radziszewski, J. G. *J. Phys. Chem. A* **2001**, *105*, 10520.
(11) Gendell, J.; Freed, J. H.; Fraenkel, George K. *J. Chem. Phys.* **1962**, *37*, 2832.
(12) Feher, G. *Phys. Rev.* **1959**, *114*, 1219.
(13) Bennett, J. E.; Mile, B.; Thomas, A. *Proc. R. Soc. London* **1966**, *A293*, 246.
(14) Kasai, P. H.; Hedaya, E.; Whipple, E. B. *J. Am. Chem. Soc.* **1969**, *91*, 4364.
(15) Hatton, W. G.; Hacker, N. P.; Kasai, P. H. *Chem. Commun.* **1990**, 227.
(16) Dixon, W. T. *Mol. Phys.* **1965**, *9*, 201.
(17) Petersson, G. A.; McLachlan, A. D. *J. Chem. Phys.* **1966**, *45*, 628.
(18) Pople, J. A.; Beveridge, D. L.; Dobosh, P. A. *J. Am. Chem. Soc.* **1966**, *90*, 4201.
(19) Adamo, C.; Barone, V.; Fortunelli, A. *J. Chem. Phys.* **1995**, *102*, 384.
(20) Mattar, S. M.; Stephens, A. D. *J. Phys. Chem. A* **2000**, *104*, 3718.
(21) Mattar, S. M. *Chem. Phys. Lett.* **1998**, *287*, 608.
(22) Improta, R.; Barone, V. *Chem. Rev.* **2004**, *104*, 1231.
(23) Lushington, G. H.; Bundgen, P.; Grein, F. *Int. J. Quantum Chem.* **1995**, *55*, 377.
(24) Bruna, P.; Grein, F. *Int. J. Quantum Chem.* **2000**, *77*, 324.
(25) Vahtras, O.; Minaev, B.; Agren, H. *Chem. Phys. Lett.* **1997**, *281*, 186.
(26) Engstrom, M.; Vahtras, O.; Agren, H. *Chem. Phys.* **1999**, *243*, 263.
(27) Schreckenbach, G.; Ziegler, T. *Theor. Chem. Acc.* **1998**, *99*, 71.
(28) Schreckenbach, G.; Ziegler, T. *J. Phys. Chem. A* **1997**, *101*, 3388.
(29) van Lenthe, E.; Wormer, P. E. S.; van der Avoird, A. *J. Chem. Phys.* **1997**, *107*, 2488.
(30) Patchkovskii, S.; Ziegler, T. *J. Chem. Phys.* **1999**, *111*, 5730.
(31) Patchkovskii, S.; Ziegler, T. *J. Phys. Chem. A* **2001**, *105*, 5490.
(32) Mattar, S. M. *J. Phys. Chem. B* **2004**, *108*, 9449.
(33) Mattar, S. M. *Chem. Phys. Lett.* **2005**, *405*, 382.
(34) Mattar, S. M.; Sanford, J.; Goodfellow, A. D. *Chem. Phys. Lett.* **2006**, *418*, 30.
(35) Neese, F. *Int. J. Quantum Chem.* **2001**, *83*, 104.
(36) Neese, F. *J. Chem. Phys.* **2001**, *115*, 11080.
(37) Neese, F. *ORCA: An Ab Initio, DFT and Semi-empirical SCF-MO Package*, version 2.4-37, 2005.
(38) Neese, F. *J. Chem. Phys.* **2005**, *122*, 34107
(39) Malkina, O. L.; Vaara, J.; Schimmelpfennig, B.; Munzarova, M.; Malkin, V. G.; Kaupp, M. *J. Am. Chem. Soc.* **2000**, *122*, 9206.
(40) Pavone, M.; Cimino, P.; DeAngelis, F.; Barone, V. *J. Am. Chem. Soc.* **2006**, *128*, 4338.
(41) Neese, F. *Magn. Reson. Chem.* **2004**, *42*, S187.
(42) *Recent Advances in Density Functional Methods*; Barone, V., Chong, D. P., Eds.; World Scientific Publishing Company: Singapore, 1996.
(43) Klamt, A.; Jonas, V.; Burger, T.; Lohrenz, J. C. W. *J. Phys. Chem. A* **1998**, *102*, 5074.
(44) Sinnecker, S.; Rajendran, A.; Klamt, A.; Diedenhofen, M.; Neese, F. *J. Phys. Chem. A* **2006**, *110*, 2235.
(45) Neese, F. *J. Chem. Phys.* **2003**, *119*, 9428.
(46) Miralles, J.; Castell, O.; Caballol, R.; Malrieu, J. P. *Chem. Phys.* **1993**, *172*, 33.
(47) Bruna, P. J.; Peyerimhoff, S. D.; Buenker, R. J. *Chem. Phys. Lett.* **1980**, *72*, 278.
(48) Pilbrow, J. R. *J. Magn. Reson.* **1984**, *58*, 186.
(49) Aasa, R.; Vanngard, T. *J. Magn. Reson.* **1975**, *19*, 308.
(50) Mattar, S. M.; Ozin, G. A. *J. Phys. Chem.* **1988**, *92*, 3511.
(51) Adamo, C.; Barone, V. *J. Chem. Phys.* **1999**, *110*, 6158.
(52) Fermi, E *Z. Phys.* **1930**, *60*, 230.
(53) Frosch, R. A.; Foley, H. M. *Phys. Rev.* **1952**, *88*, 1337.
(54) Mattar, S. M.; Sammynaiken, R. *J. Chem. Phys.* **1997**, *106*, 1094.
(55) Mattar, S. M.; Sammynaiken, R. *J. Chem. Phys.* **1997**, *106*, 1080.
(56) Mattar, S. M. *Chem. Phys. Lett.* **1999**, *300*, 545.